Journal of Materials Chemistry C

ROYAL SOCIETY OF CHEMISTRY

PAPER

View Article Online
View Journal | View Issue

Cite this: J. Mater. Chem. C, 2023, 11, 10282

Band gap tuning through cation and halide alloying in mechanochemically synthesized $Cs_3(Sb_{1-x}Bi_x)_2Br_9$ and $Cs_3Sb_2(I_{1-x}Br_x)_9$ solid solutions†

Giulia Giovilli,[a] Benedetta Albini, [b] Virginia Grisci,[c] Sara Bonomi,[a] Marco Moroni,[a] Edoardo Mosconi, [d] Waldemar Kaiser, [d] Filippo De Angelis,[cdef] Pietro Galinetto[b] and Lorenzo Malavasi *[a]

Received 28th April 2023,
Accepted 5th June 2023

DOI: 10.1039/d3tc01492d

rsc.li/materials-c

Modulation of the optical properties of lead-free defective perovskites can contribute to the design of optimized materials for several applications ranging from photodetection to photocatalysis. Here, we explored two novel alloying strategies in $Cs_3Sb_2Br_9$ by preparing, through mechanochemical synthesis, Sb/Bi and Br/I mixed systems. An unexpected band gap bowing has been observed in alloyed Sb/Bi compositions, showing lower absorption edges with respect to pure compounds. Such behavior has been computationally modelled suggesting the presence of local aggregates as the source of such a reduction of the band gap. Further modulation of the optical properties has been achieved by halide alloying showing a progressive red-shift by increasing the iodide content. In both cases, full solubility at the solid state has been determined by means of diffraction and Raman spectroscopy. Overall, this study proposes and rationalizes doping strategies in the $Cs_3Sb_2Br_9$ defective perovskite, achieved through the use of a sustainable synthetic procedure such as mechanochemistry.

Introduction

In the last decade, metal-halide perovskites (MHPs) have grown to be the most promising material class for future photovoltaic (PV) devices. While their huge potential is out of the question, recent experimental and computational research expands beyond the class of lead-halide perovskites exploring chemical and structural phase spaces of MHPs and perovskite derivatives.[1] Several structually diverse systems are now under investigation, including, for example, 3D, 2D, and double perovskites, targeting applications beyond PV, *e.g.* photodetection and photocatalysis.[2–11]

The expansion of the discovered material space of MHPs has recently moved towards the investigation of lead-free systems in order to overcome the concerns related to Pb-toxicity. While effective alternatives for PV applications rely mostly on tin-based compositions, several other phases containing different metals such as Bi, Sb, Cu, and Ge have been discovered and investigated.[12–19] In many cases, such perovskites result ill-suited for PV devices but possess very appealing optoelectronic properties, which can be exploited in other applications. Among these systems, bismuth- and antimony-based perovskite derivatives of general formula $Cs_3M_2X_9$ (M = Bi, Sb; X = Br, I) have shown strong technological potential, in particular in the area of photocatalysis (both for solar fuel generation and organic synthesis) and photodetection.[20–36]

Bismuth-based defect-ordered perovskites have been an object of more intense studies compared to the corresponding Sb systems, notwithstanding their appealing optoelectronic properties such as high carrier mobility, low trap density, and long diffusion length. As a matter of fact, $Cs_3Sb_2Br_9$ millimeter-sized single crystals and nanoflakes have been applied in the fabrication of photodetectors with excellent performance in terms of responsivity and detectvity.[37,38] Good photodetectors based on $Cs_3Sb_2Br_9$ have also been prepared by means of a

[a] Department of Chemistry and INSTM, University of Pavia, Via Taramelli 16, Pavia, 27100, Italy
[b] Department of Physics, University of Pavia, Via Bassi 6, Pavia, 27100, Italy. E-mail: lorenzo.malavasi@unipv.it; Tel: +39 382 987921
[c] Department of Chemistry, Biology and Biotechnology, University of Perugia and INSTM, Via Elce di Sotto 8, Perugia 06123, Italy
[d] Computational Laboratory for Hybrid/Organic Photovoltaics (CLHYO), Istituto CNR di Scienze e Tecnologie Chimiche "Giulio Natta" (CNR-SCITEC), Via Elce di Sotto 8, Perugia 06123, Italy
[e] Department of Mechanical Engineering, College of Engineering, Prince Mohammad Bin Fahd University, P.O. Box 1664, Al Khobar, 31952, Saudi Arabia
[f] SKKU Institute of Energy Science and Technology (SIEST) Sungkyunkwan University, Suwon, 440-746, Korea

† Electronic supplementary information (ESI) available: Experimental conditions, SEM images, additional XRD patterns, and computational details. See DOI: https://doi.org/10.1039/d3tc01492d

chemical vapor deposition technique.[39] $Cs_3Sb_2Br_9$ and $Cs_3Sb_2I_9$ were also revealed to be suitable candidates for photocatalytic applications and in this respect have been, for example, applied in photocatalytic carbon dioxide reduction, water splitting, and aromatic C-H bond activation.[40–44] Some efforts have also been made towards the possible use of these defect-ordered perovskites in the manufacturing of solar cells. $Cs_3Sb_2I_9$ has been preferentially used for PV due to its suitable band gap of around 2 eV, providing good stability but relatively low efficiencies of around 2–3%.[45–47]

While there is clearly a relevant interest in Sb-based materials, many of their fundamental features still need to be explored: for example synthetic procedures, band gap tuning by metal or halide alloying, and their electronic structure. Considering the structural and optoelectronic similarity with Bi-based analogues, which have been more deeply investigated, it appears that some tuning strategies of the photophysical properties of Sb materials should be clarified to enlarge the plethora of lead-free perovskite derivatives. For example, the preparation of mixed Sb/Bi phases of vacancy ordered perovskites has not been reported in the current literature but there is a strong motivation to investigate such a system. Indeed, a recent work on the $Cs_2Ag(Sb_xBi_{1-x})Br_6$ double perovskite solid solution has demonstrated a nonlinear trend of the band gap value as a function of x, providing mixed compositions with lower values with respect to $Cs_2AgBiBr_6$ and $Cs_2AgSbBr_6$.[48] However, the possibility of successfully preparing a continuous solid solution within the vacancy-ordered $Cs_3(Sb_{1-x}Bi_x)_2Br_9$ system is still to be verified. The choice of a suitable synthetic route for these Sb/Bi materials is critical due to the low solubility of halide precursors posing strong limitations for traditional synthesis procedures applied to MHPs. A viable choice could be the use of mechanochemistry which has been recently applied to Bi-based systems but never to Sb-containing perovskites or mixed compositions. Finally, the halide alloying strategy to modulate the optical properties of perovskites is still to be investigated in Sb vacancy-ordered materials.

Based on the above considerations, in this work we carried out the mechanochemical synthesis of the $Cs_3(Sb_{1-x}Bi_x)_2Br_9$ and $Cs_3Sb_2(I_{1-x}Br_x)_9$ systems ($0 \leq x \leq 1$) to understand the effect of Sb/Bi and I/Br alloying on the structural and optical properties. For both alloying routes, we employ mechanochemistry as the main preparation technique to verify its suitability for Sb-based systems and its ability to provide phase-pure mixed compositions.

Results and discussion

$Cs_3(Sb_{1-x}Bi_x)_2Br_9$ system

Powdered samples of the $Cs_3(Sb_{1-x}Bi_x)_2Br_9$ system for x = 0, 0.1, 0.2, 0.4, 0.6, 0.8, 0.9, and 1 have been prepared using a planetary ball miller according to the experimental conditions reported in the Experimental section (see the ESI†). Fig. 1 shows the appearance of the eight samples prepared from $Cs_3Sb_2Br_9$ (left) to $Cs_3Bi_2Br_9$ (right).

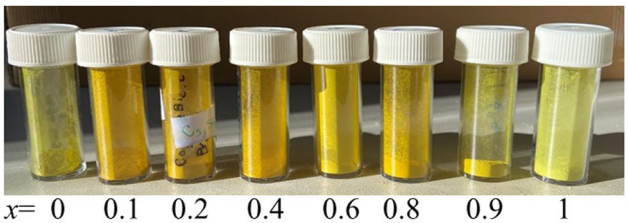

Fig. 1 Photograph of the samples of $Cs_3(Sb_{1-x}Bi_x)_2Br_9$ solid solution.

Fig. 2 presents the room temperature (RT) X-ray diffraction (XRD) patterns collected for all the samples reported in Fig. 1. Samples have been measured both with Cu-K radiation (Fig. 1) and with Mo-K radiation (Fig. S1a and b, ESI†) to provide the most reliable structural results on these novel samples. Compositions (expressed as x) in Fig. 1 refer to the effective stoichiometries determined by microprobe analysis (see later in the text). All the samples are single phase and in agreement with the hexagonal symmetry of $P\bar{3}m1$, the space group that describes the two end members, namely $Cs_3Sb_2Br_9$ and $Cs_3Bi_2Br_9$. A superposition of the reference structure model for these last two samples and the experimental patterns are shown in Fig. 2b and c, respectively.

According to these results, the mechanochemical synthetic procedure was effective in preparing single-phase materials for both of the two stoichiometric compositions, $Cs_3Sb_2Br_9$ and $Cs_3Bi_2Br_9$, and for the mixed Sb/Bi samples. A green and sustainable synthetic approach such as this has never been applied to Sb-based defective perovskites nor to B-site mixed compositions, while a previous report on its effective use for the preparation of $Cs_3Bi_2Br_9$ is reported in the current literature.[49]

The morphology and chemical composition of the samples has been determined by means of scanning electron microscopy (SEM) and microprobe analysis. Images of the sample morphology are provided in Fig. S2 (ESI†). As a consequence of the mechanochemical synthesis, the samples do not possess a well-defined morphology, as occurs in solution-chemistry synthesis, and grains with various shapes and dimensions (in the micron and sub-micron range) are observed. Elemental analysis by energy dispersive spectroscopy (EDS) confirmed a good agreement with the nominal compositions (see Table 1). In the rest of the paper, we will make use of the effective compositions instead of the nominal ones when discussing the experimental results.

The XRD patterns have been refined using the Rietveld method. The lattice parameters determined are reported in Table 1, while Fig. 3a and b show their trend together with lattice volume as a function of x (Bi-content).

The linear trend of the lattice volume reported in Fig. 3c agrees with Vegard's law for solid solution, confirming the complete solubility of Sb/Bi in the lattice. This result could be anticipated based on the similar ionic radii between Sb^{3+} and Bi^{3+} ions and the same crystal structure of the two end-members.

A Raman investigation has been performed, focusing on the low energy part of the Raman activity, *i.e.* in the range 25–250 cm^{-1}. At a first glance, the single-phase of the end-members samples is confirmed, as reported in Fig. 4a. Indeed, the Raman spectrum of

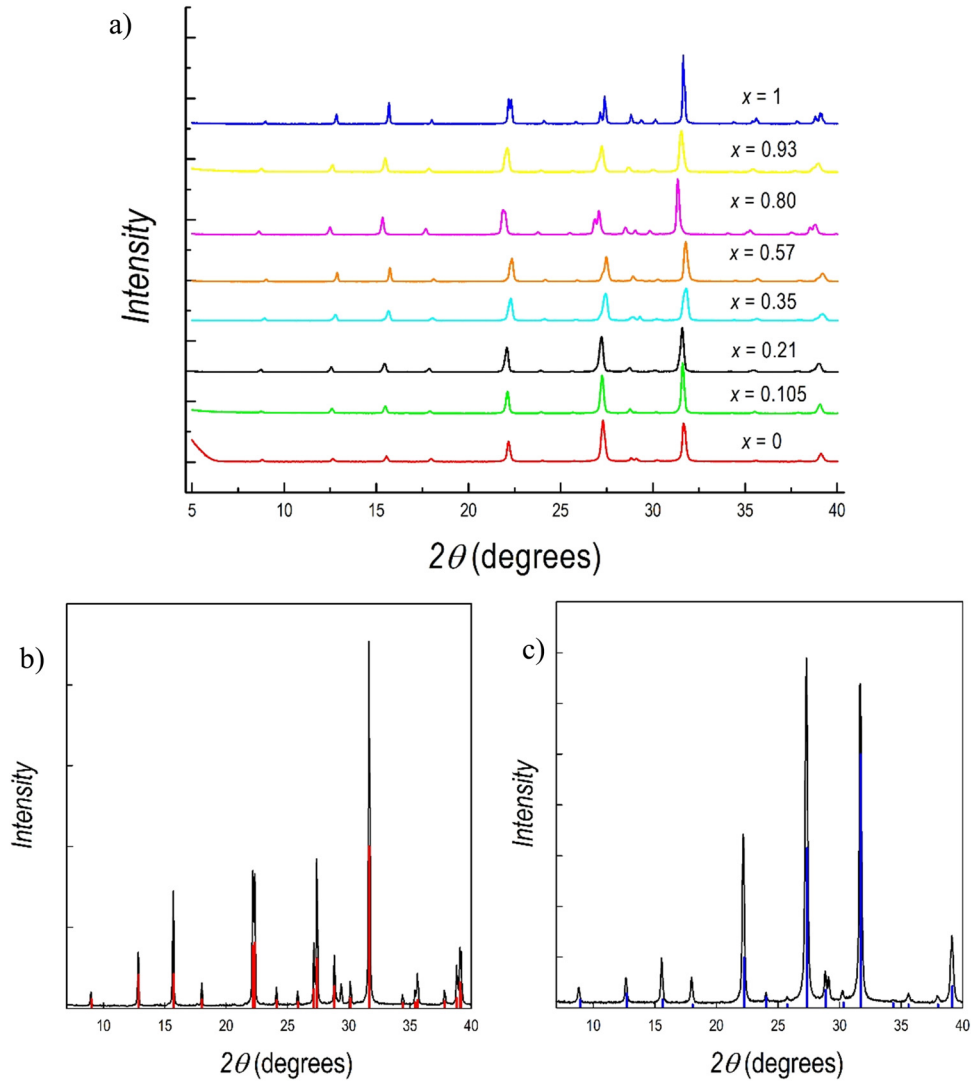

Fig. 2 (a) XRD patterns of a $Cs_3(Sb_{1-x}Bi_x)_2Br_9$ solid solution as a function of x; (b) diffraction pattern of $Cs_3Bi_2Br_9$ superimposed to the calculated pattern of the hexagonal structure (vertical red lines); and (c) diffraction pattern of $Cs_3Sb_2Br_9$ superimposed to the calculated pattern of the hexagonal structure (vertical blue lines).

Table 1 Composition determined by microprobe analysis, lattice parameters and band gap (BG) values for the $Cs_3(Sb_{1-x}Bi_x)_2Br_9$ samples

Nominal (x)	Effective (x)	$a = b$ (Å)	c (Å)	Volume (Å^3)	Direct BG (eV)	Indirect BG (eV)
0	0	7.9015(3)	9.7119(4)	525.12(4)	2.50	2.31
0.1	0.105	7.9065(3)	9.7227(4)	526.37(4)	2.34	2.07
0.2	0.21	7.9090(3)	9.7284(4)	527.01(4)	2.31	2.03
0.4	0.35	7.9126(3)	9.7523(4)	528.79(4)	2.33	2.04
0.6	0.57	7.9326(3)	9.7907(4)	533.55(4)	2.34	2.11
0.8	0.80	7.9502(3)	9.8261(4)	537.86(4)	2.39	2.12
0.9	0.93	7.9580(3)	9.8382(4)	539.58(4)	2.43	2.17
1	1	7.9666(3)	9.8422(4)	540.97(4)	2.58	2.46

the $Cs_3Bi_2Br_9$ sample clearly shows the characteristic modes at 165 and 190 cm^{-1}, due to the bond vibrations inside the octahedral cage, $BiBr_6$, as already described in our previous work.[36]

In analogy with $Cs_3Bi_2Br_9$, $Cs_3Sb_2Br_9$ Raman response presents, qualitatively, the same spectral fingerprints: a broadened structure centered at about 70 cm^{-1}, clearly resulting from the overlapping of different modes, and two sharp and symmetric mode peaks at 182 and 210 cm^{-1}, resulting from the Sb-Br bond vibrations in the octahedral unit $SbBr_6$. The proper assignment of the mode symmetry seems to be controversial.

Indeed, in ref. 50, the mode at 210 cm^{-1} is given an A_{1g} symmetry and the one at 182 cm^{-1} an E_{1g} one, while in ref. 37, the opposite is given.[37,50] However, besides this discrepancy, the two vibrational modes foresee the displacement of both Sb and Br atoms, as it is for the $Cs_3Bi_2Br_9$ sample.[50] The Raman spectra collected for the whole set of samples, moving from $Cs_3Bi_2Br_9$ to $Cs_3Sb_2Br_9$, in the region between 25 and 280 cm^{-1} are reported in Fig. S3 (ESI†). It's clear that the progressive substitution of Sb atoms with heavier Bi ones highly affects the modes above 150 cm^{-1}. From these data we derived a color map (Fig. 4b) showing the energy changes experienced by the A_{1g} and E_g modes by gradually varying the relative abundance of Sb

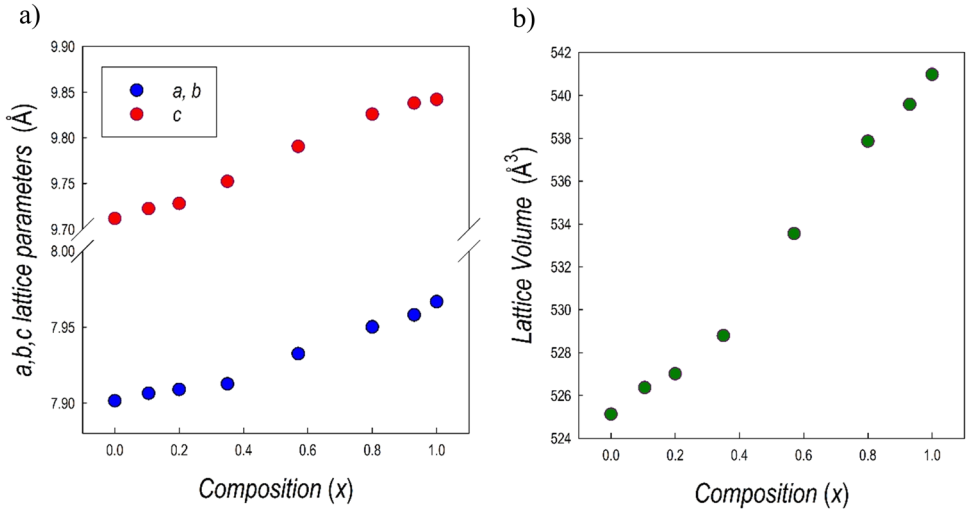

Fig. 3 Trend of (a) $a = b$ and c lattice parameters, (b) cell volume for the samples of the $Cs_3(Sb_{1-x}Bi_x)_2Br_9$ solid solution as a function of x.

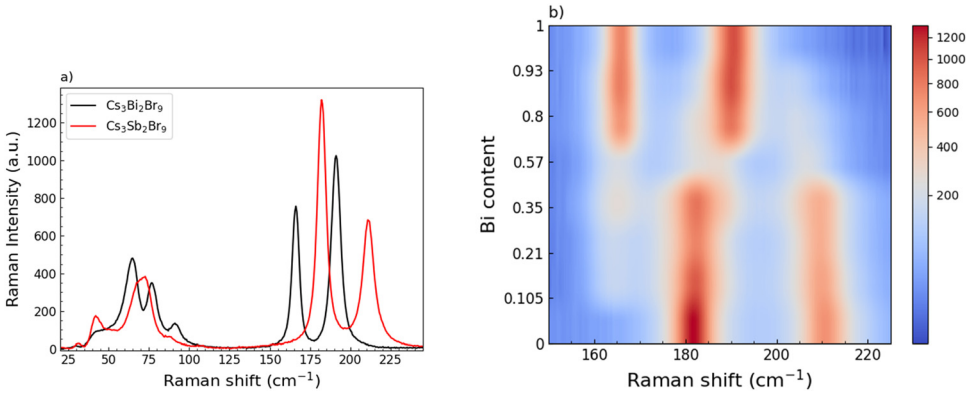

Fig. 4 (a) Comparison between room temperature (RT) Raman spectra of the end-members. (b) Color map reporting the modes intensity of the sample spectra in the range between 150 and 225 cm^{-1} as a function of Bi content (we applied a power-law normalization to remap the colors, to increase the contrast and better point out the change in the mode position).

and Bi. The energy changes of the main Raman bands indicate a clear two-mode behavior where, for a small amount of Bi, the peculiar modes of the $Cs_3Bi_2Br_9$ sample already affect the collected spectra, with a constant increase of their intensities as the number of $BiBr_6$ units progressively replace the $SbBr_6$ ones. The increasing in Bi amount causes a redshift of the Raman bands, particularly pronounced for the mode at 210 cm^{-1}, in agreement with a progressive cell expansion and resulting increase of the interatomic distance, as pointed out by the XRD measurements.

The crossover between Bi-rich and Sb-rich systems is also well evidenced in Fig. S4a (ESI†) where the intensity of the mode at about 165 cm^{-1} characteristic of $Cs_3Bi_2Br_9$ and the one at 210 cm^{-1} of $Cs_3Sb_2Br_9$ are plotted as a function of Bi content: as the former increases, the latter decreases. In Fig. S4b (ESI†), the spectrum for the $x = 0.57$ sample is reported together with the result from the best-fitting procedure using four Lorentzian curves according to the above mentioned two-mode behavior.

Fig. 5a reports the UV-Vis reflectance spectra collected for the whole series of samples of the $Cs_3(Sb_{1-x}Bi_x)_2Br_9$ solid solution. It can be seen that the absorption edges of the two stoichiometric compounds, *i.e.* the red spectrum for $Cs_3Sb_2Br_9$ and the blue spectrum for $Cs_3Bi_2Br_9$, are blue-shifted with respect to all the mixed compositions. Bi-and Sb-based defective perovskites present a dual direct–indirect transition, which has been previously observed and also described from a computational point of view.[51,52] The direct band gap transition derives from the promotion of electrons from the valence band (VB) to the conduction band (CB) followed by the excited electrons relaxing to the CB minimum and recombining with the holes in the VB maximum. If this process occurs with the assistance of phonons, an indirect band gap transitions occurs. The values of the direct and indirect band gaps, determined from the Tauc plots (reported in Fig. S5, ESI†), are shown in Fig. 5b as a function of x.

The values of direct and indirect band gaps for $Cs_3Sb_2Br_9$ and $Cs_3Bi_2Br_9$ are in agreement with those previously reported in current literature.[34,36,39,51] By looking at Fig. 5b, a significant bowing of the band gap in mixed compositions is observed. This result is unexpected since, in general, metal ion replacement in

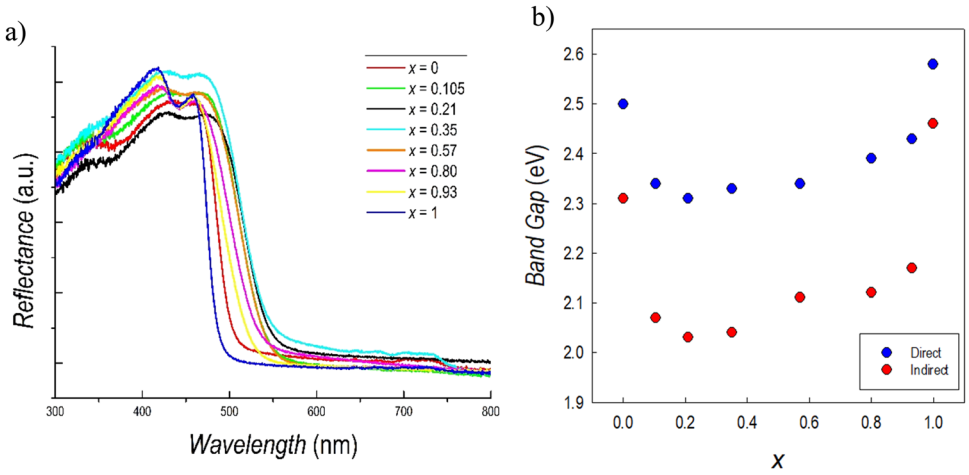

Fig. 5 (a) Reflectance spectra and (b) trend of the band gaps of the $Cs_3(Sb_{1-x}Bi_x)_2Br_9$ solid solution.

solid solution provides a scaling of the band gap obeying Vegard's law. The reduction of the band gap (direct) in mixed compositions is relevant, reaching a minimum value of about 2.35 eV when x is around 0.2–0.4. The same trend of band gap bowing is observed for the indirect band gap. Such a trend has never been observed before in any defective perovskite, but has been reported for the double perovskite system $Cs_2AgSb_{(1-x)}Bi_xBr_6$ and attributed to chemical rather than structural effects.[48] In our case, we cannot exclude a synergistic effect due to the coexistence of mass disorder and microscopic strain, as it is expected in a two-mode scenario evidenced by Raman data.[48] The present results corroborate the strategy of band gap tuning by Sb/Bi mixing, which seems to be general, considering the structural difference between defective perovskite and double perovskites, and therefore related to the peculiar electronic properties of antimony and bismuth in mixed compositions.

To understand the unexpected change in band gap, density functional theory (DFT) calculations have been performed for the reference systems $Cs_3Sb_2Br_9$ and $Cs_3Bi_2Br_9$ as well as for mixed $Cs_3(Sb_{0.5}Bi_{0.5})_2Br_9$. Ionic positions of the three systems were obtained by PBE+D3 geometry optimization, followed by refined electronic structure calculations using the hybrid HSE06 functional including spin–orbit coupling (see the ESI† for computational details). The indirect bandgap and first direct transition of $Cs_3Bi_2Br_9$ ($Cs_3Sb_2Br_9$) were calculated to be 2.97 (2.91) and 3.10 (2.96) eV, respectively (see Table 2). Previous GW-BSE calculations showed large exciton binding energies of ~300 meV, which are not captured in our DFT calculations.[53] Correcting our DFT results by the large exciton binding energies results in a fair agreement with the experimental band gap values.

Table 2 Theoretical and experimental values of the direct and indirect band gap energies for the pure $Cs_3Sb_2Br_9$ and $Cs_3Bi_2Br_9$ compounds and for the mixed $Cs_3(Sb_{0.5}Bi_{0.5})_2Br_9$. All theoretical values are on the HSE06+-SOC level of theory, neglecting excitonic effects on the absorption energies which are of ~300 meV[53]

	$Cs_3Sb_2Br_9$	$Cs_3(Sb_{0.5}Bi_{0.5})_2Br_9$	$Cs_3Bi_2Br_9$
D/I	I	I	I
BG direct	2.96	2.71	3.10
BG indirect	2.91	2.59	2.97
Exp. direct	2.50	2.34	2.58
Exp. indirect	2.31	2.11	2.46

For the pure Sb and Bi species, the contribution of valence band is primarily given from bromine 4p orbitals with slight metal contribution, while the conduction band is mainly due to the metal cation (for Sb 5p orbitals and Bi 6p orbitals) and its interaction with bromine 4p orbitals, see Fig. 6a. Moving to the mixed Bi/Sb material, we observe substantial differences depending on the arrangement of the metal ions. The fully mixed system, with alternating $SbBr_6$ and $BiBr_6$ octahedra, interestingly shows a negligible difference in band gaps, with indirect and direct bandgaps of 2.90 and 3.00 eV, compared to the pure Sb and Bi species, see Fig. S6 (ESI†). When we consider aggregates of Sb and Bi, see Fig. 6b, we observe a decrease to 2.59 and 2.71 eV of the indirect and direct band gaps, respectively (*cf.* Fig. 6a). In terms of stability, the two models show the same energy, suggesting that both appear equally in the crystal structure. This clearly suggests that the band-gap decrease found experimentally for the mixed Sb/Bi material is associated with the presence of this kind of aggregate. As a matter of fact, considering the energy alignment in the density of states (Fig. 6a), we found, moving from $Cs_3Bi_2Br_9$ to $Cs_3SbBiBr_9$, an upshift in the VB and CB of 0.52 eV and of 0.15 eV, respectively. In contrast, the VB is nicely aligned with the $Cs_3Bi_2Br_9$ compound, showing a shift of only 0.21 eV, compared to a large CB shift of 0.53 eV. The DOS of mixed $Cs_3SbBiBr_9$ shows that the VB is mainly associated with Br alongside a slight Sb contribution, while the CB is made up of Bi and Br states in a similar ratio. Consequently, we can explain the drop in band gap upon Sb/Bi alloying by the formation of $SbBr_6$ and $BiBr_6$ aggregates, which dominate the VB and the CB, respectively, as schematically shown in Fig. 6c. This is the first report of such an effect in this Sb/Bi vacancy ordered perovskite alloys, while an analogous trend was found for the double perovskite system $Cs_2AgSb_xBi_{(1-x)}Br_6$.[48]

Band gap bowing of mixed metal perovskites has been observed in Pb/Sn perovskites and attributed to a chemical

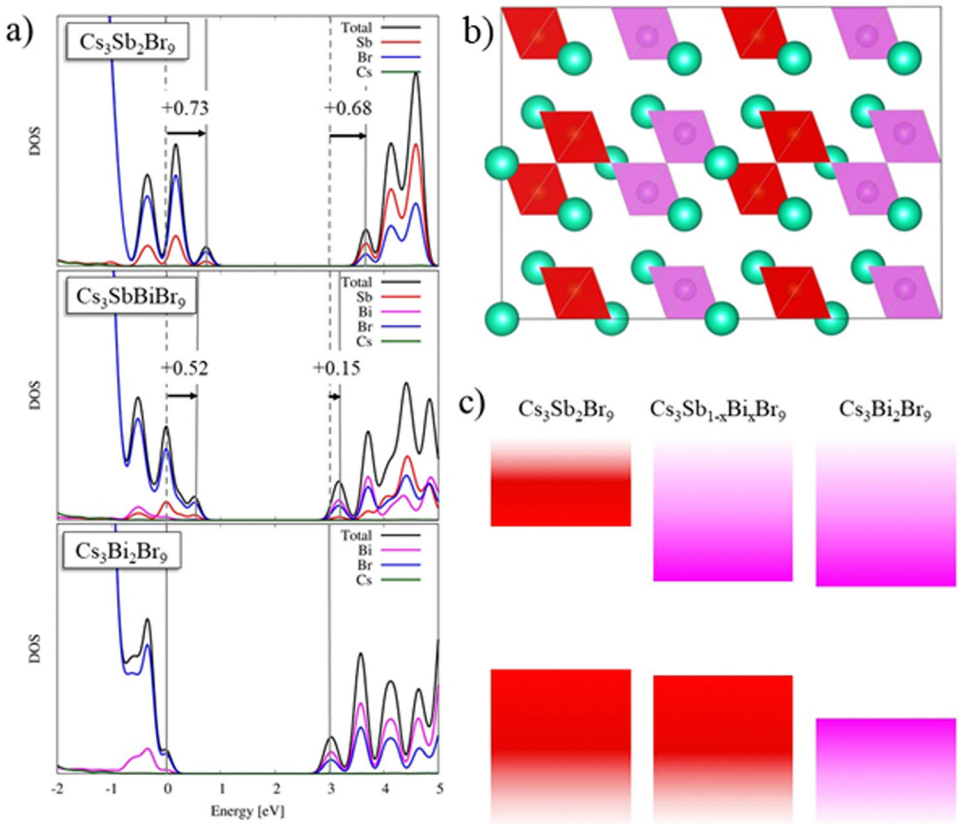

Fig. 6 (a) Calculated DOS for (top) $Cs_3Sb_2Br_9$, (middle) $Cs_3SbBiBr_9$, and (bottom) $Cs_3Bi_2Br_9$. All DOS are aligned with respect to the valence band maximum of $Cs_3Bi_2Br_9$. (b) Structural representation of the mixed $Cs_3SbBiBr_9$ system, showing aggregation of Sb- and Bi-centered octahedra. $SbBr_6$ and $BiBr_6$ octahedra are represented by red and pink polyhedra, respectively. Cs atoms are shown in green. For simplicity, Br atoms are removed. (c) Schematics of the band contributions upon mixing in $Cs_3(Sb_{0.5}Bi_{0.5})_2Br_9$: Conduction band edge is dominated by Bi aggregates, while the valence band edge is dominated by Sb aggregates.

effect: mismatch in energy between s and p atomic orbitals of the two metals.[54] A similar interpretation also holds for the present $Cs_3(Sb_{1-x}Bi_x)_2Br_9$ solid solution where a mismatch in energy between s and p atomic orbitals of Sb and Bi is found. It is of relevance to report here this novel tuning strategy for defective perovskites which allows achieving significantly lower band gap values through metal alloying instead of the usual halide mixing, known to be the main strategy for modulating the absorption edge in these systems.[25,26,36]

$Cs_3Sb_2(Br_{1-x}I_x)_9$ system

We further explored alloying strategies by tuning the halide content Br/I of the $Cs_3Sb_2Br_9$ perovskite. While such a strategy has been explored for the Bi analogue, no studies are reported for the Sb-based composition.[25,36] For this purpose, samples of the $Cs_3Sb_2Br_{9-x}I_x$ system with x = 0 (also reported above), 2.5, 4.5, 6.5, and 9 have been synthesized by means of mechanochemistry according to the experimental conditions reported in the ESI.† Photographs of the five samples are displayed in Fig. 7a. XRD patterns for the whole series are shown in Fig. 7b. For the $Cs_3Sb_2I_9$ perovskite two different polymorphs have been previously reported, namely the layered modification with *e.g.* (space group) $P\bar{3}m1$ (analogous to $Cs_3Sb_2Br_9$, see above) and the dimer modification with the space group $P6_3/mmc$, featuring SbI_6 octahedra fused into $Sb_2I_9^{3-}$ dimers through sharing of their triangular faces.[55] According to the literature, the dimer form is synthesized from solution using a polar solvent, whereas the layered form is obtained from a solid state reaction.[56] However, the present synthetic approach has never been reported before for $Cs_3Sb_2I_9$, and additional information on the stability of the different polymorphs has been obtained. According to Fig. 7c, reporting the XRD patterns of $Cs_3Sb_2I_9$ perovskite against the expected structure for the $P\bar{3}m1$ space group, we could obtain the layered modification through mechanochemistry. Nonetheless, this was possible after optimizing the synthesis approach in terms of milling cycles and time. By way of an example, Fig. S7 (ESI†) presents the pattern of $Cs_3Sb_2I_9$ obtained at 400 rpm with 6 milling cycles which shows a mixed sample composed of the two polymorphs. The present results show the first successful synthesis of layered $Cs_3Sb_2I_9$ by means of a mechanochemistry approach.

Fig. 7b presents the RT Cu-K XRD patterns of all the samples of the $Cs_3Sb_2Br_{9-x}I_x$ system, all in agreement with the $P\bar{3}m1$ *e.g.* A clear shift of all the peaks towards lower angles is evident by increasing the iodide content (x), in agreement with the unit-cell volume increase. All the samples result in being single-phase

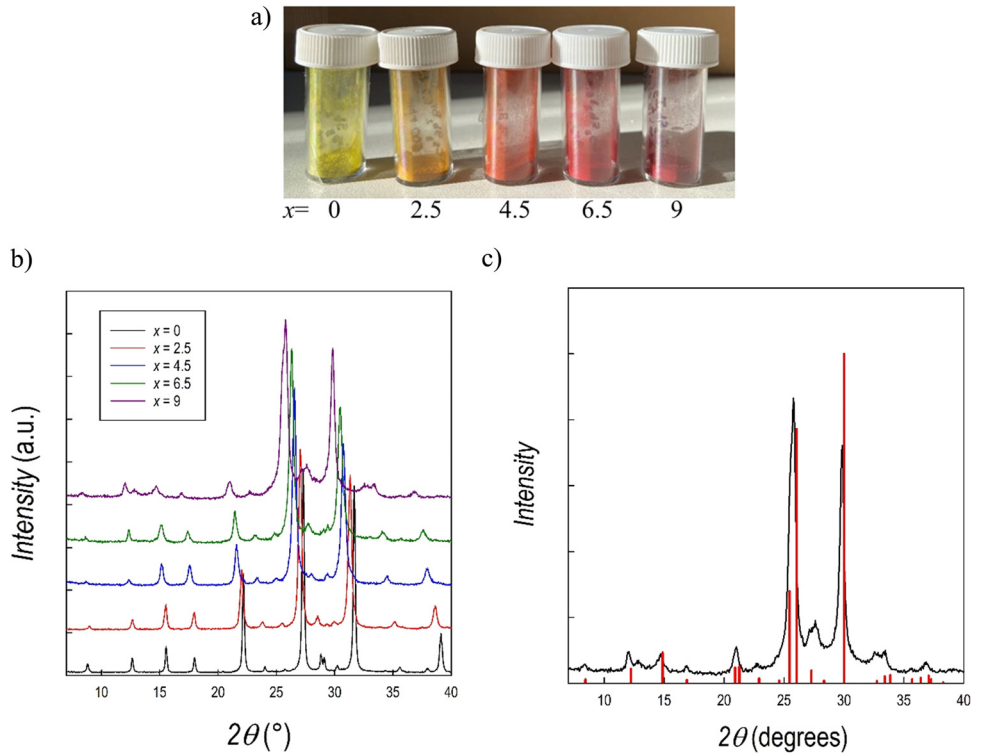

Fig. 7 (a) Photograph of the samples of $Cs_3Sb_2Br_{9-x}I_x$ solid solution; (b) XRD patterns of the $Cs_3Sb_2Br_{9-x}I_x$ solid solution, (c) XRD pattern of $Cs_3Sb_2I_9$ against the calculated structure of the layered polymorph (*e.g.* $P\bar{3}m1$)

and the patterns have been refined using the Rietveld method: lattice parameters and cell volume trend as a function of x are shown in Fig. 8 and listed in Table 3. Microprobe analysis resulted in a perfect agreement (within the e.s.d.) between nominal and effective halide contents.

All the data follow a linear trend as a function of the iodide content, according to Vegard's law, confirming the formation of a continuous solid solution in this system, as with the analogous Bi-based system.[25,36]

The observed unit-cell expansion together with the progressive substitution of Br atoms with a heavier one leads again to a clear redshift of the Raman modes, more pronounced with respect to what is observed when Bi/Sb are replaced at the B sites, as described above. From Fig. 9 this behavior is particularly evident for the mode at 210 cm^{-1} characteristic of the $Cs_3Sb_2Br_9$ structure: its center shifts up to 185 cm^{-1} for the x = 6.5 sample, then it completely disappears in the $Cs_3Sb_2I_9$ compound.

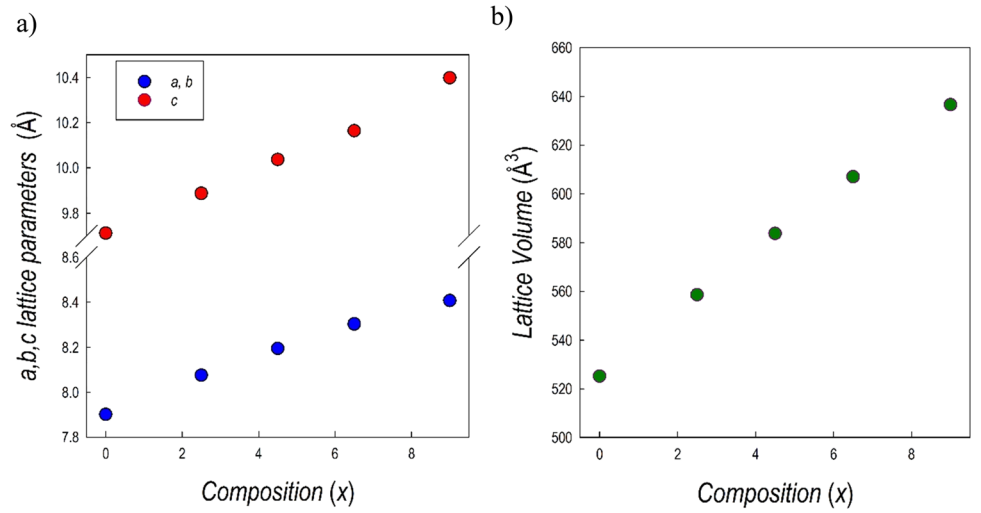

Fig. 8 Trend of (a) a = b and c lattice parameter, and (b) cell volume for the samples of the $Cs_3Sb_2Br_{9-x}I_x$ solid solution as a function of x.

Table 3 Lattice parameters and band gap (BG) values for the $Cs_3Sb_2Br_{9-x}I_x$ samples

X	$a = b$ (Å)	c (Å)	Volume (Å^3)	Direct BG (eV)	Indirect BG (eV)
0	7.9015(3)	9.7119(4)	525.12(4)	2.50	2.31
2.5	8.0760(3)	9.8875(4)	558.49(4)	2.21	1.87
4.5	8.1950(3)	10.0368(4)	583.74(4)	2.02	1.71
6.5	8.3037(3)	10.1642(4)	606.95(4)	1.98	1.70
9	8.4074(3)	10.3995(4)	636.61(4)	1.95	1.67

Moving from one end-member to the other, gradual changes are observed, but it's harder to recognize a two-mode behavior, probably as a result of higher disorder in the chemical distribution related to the specific site involved in the substitution. Moreover, as a consequence of the later-discussed bandgap red-shift, the Raman intensity of the x = 4.5, 6.5 and 9 samples are strongly increased: indeed, these three samples start absorbing at 638 nm, namely the incident laser wavelength used to perform the characterization.

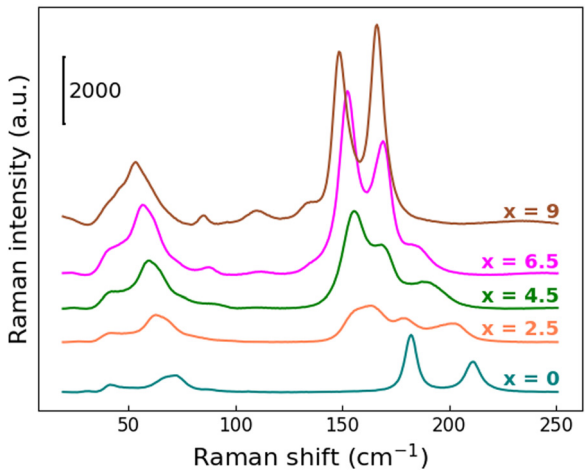

Fig. 9 RT Raman spectra in the region between 25 and 250 cm^{-1} for $Cs_3Sb_2Br_{9-x}I_x$ solid solutions as a function of x.

Finally, the Raman activity of the $Cs_3Sb_2I_9$ sample is consistent with the literature.[52,57] The spectrum is dominated by two intense features at 148.9 and 166.3 cm^{-1}, once again assigned to the A_{1g} and E_g vibrational modes, involving both I and Sb atoms in the octahedral unit. Other less pronounced modes at 135.2 cm^{-1}, 110.1 cm^{-1} and 85.3 cm^{-1}, together with a broad feature at about 50 cm^{-1}, are present in the spectrum. According to ref. 50 and 56, the lowest frequency modes, 85.3 cm^{-1} and the structure at 50 cm^{-1}, are assigned to Sb–I bending and Sb–I–Sb interactions, respectively.

UV-vis absorption spectroscopy measurements on the $Cs_3Sb_2Br_{9-x}I_x$ system are reported in Fig. 10a. There is a clear red shift obtained by increasing the amount of iodide, with a more pronounced effect up to x = 4.5. The trend of direct and indirect band gap values as a function of iodide content is shown in Fig. 10b.

The values for the two end members are in agreement with those reported in current literature.[41,43] On the other hand, no previously reported data for Br/I mixed samples are available. Data in Fig. 10b show a relevant initial reduction of the (direct) band gap from about 2.5 to 2.1 eV (at 50% of Br and I), followed by a smoother reduction of the band gap up to about 2.0 eV, showing again a bowing of the E_g. A similar alloying strategy was investigated for the $Cs_3Bi_2Br_{9-x}I_x$ defective perovskites showing as well a degree of band-gap bowing which is, however, less pronounced than the present Sb-based perovskites.[25,36]

Conclusions

In the present work we explored two novel alloying strategies for the $Cs_3Sb_2Br_9$ defective perovskites, namely Sb/Bi and Br/I mixing. All the samples have been prepared for the first time (for these systems) following a mechanochemistry route, indicating its suitability in providing single-phase materials and in preserving the stoichiometry (for both stoichiometric and alloyed samples). The variation of cell parameters for $Cs_3(Sb_{1-x}Bi_x)_2Br_9$ follows Vegard's law indicating the formation of a continuous

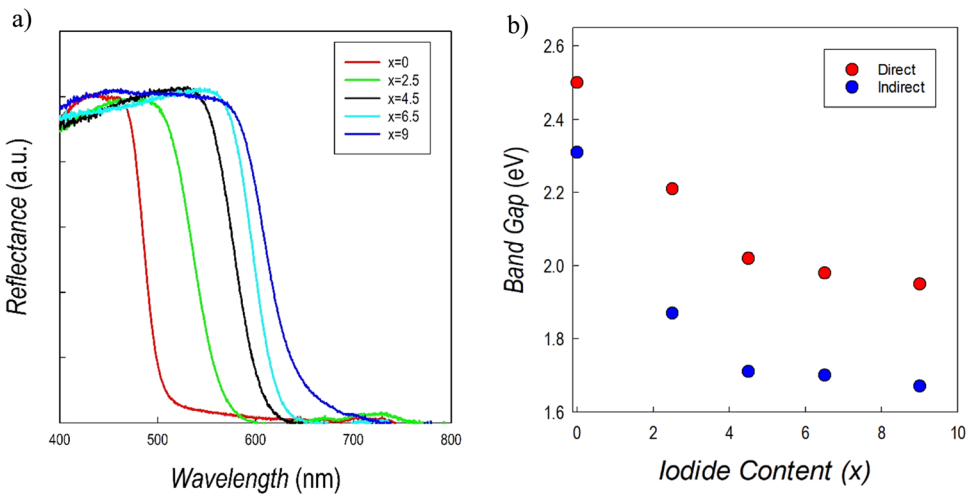

Fig. 10 (a) Reflectance spectra and (b) trend of the band gaps of the $Cs_3Sb_2Br_{9-x}I_x$ solid solution.

solid solution. On the other hand, the trend of both direct and indirect band gaps shows a significant bowing and reduction for mixed Sb/Bi compositions, allowing access to band gap values lower than the two end-members, namely $Cs_3Sb_2Br_9$ and $Cs_3Bi_2Br_9$. This behavior has been modelled by DFT indicating that, for mixed systems, Sb and Bi aggregates control different regions of the electronic structure, showing a Sb-like valence band edge and a Bi-like conduction band edge, causing the drop in the band gap at all mixing ratios.

For the $Cs_3Sb_2Br_{9-x}I_x$ system we reported the first successful mechanochemical synthesis of the layered polymorph of the $Cs_3Sb_2I_9$ perovskite, previously obtained only *via* a conventional solid state reaction. The Br/I alloying resulted in a linear expansion of the unit cell by increasing the I content, also confirming, in this case, a full solubility of the two halides in the lattice. Absorption spectroscopy indicates a progressive redshift by increasing x, with a pronounced bowing of the band gap from $x = 4.5$ to $x = 9$.

For both $Cs_3(Sb_{1-x}Bi_x)_2Br_9$ and $Cs_3Sb_2Br_{9-x}I_x$ the Raman inspection allowed confirming the single-phase structure of all the end-members. Moreover, the reported results, confirmed by XRD evidence, point out a redshift of the modes as a consequence of the cell expansion and the substitution of heavier ions that enlarged the reduced mass of the vibrational unit. The Raman features of the mixed samples are consistent with a two-mode behavior and the mixed phonon landscape, which can, in turn, play an active role in the electronic response.

The present results provide a novel sustainable synthetic route for the preparation of Sb-based defective perovskites and, more importantly, two alloying strategies which allow tuning the band gap in most of the visible spectrum, also providing the first evidence of band gap reduction by metal mixing (Sb/Bi) in a defective perovskite structure. Such an effect has been previously observed only in double perovskites ($Cs_2AgSb_xBi_{(1-x)}Br_6$), suggesting its possible universal character which is worth of further exploration in other related systems.

Conflicts of interest

There are no conflicts to declare.

Acknowledgements

LM acknowledges support from the Ministero dell'Università e della Ricerca (MUR) and the University of Pavia through the program ''Dipartimenti di Eccellenza 2023–2027.'' EM and WK wish to thank project Ricerca@CNR PHOTOCAT (CUP B93C21000060006) and the POR H2 project, L.A.1.1.35 (CUP B93C22000630006). This work has been further funded by the European Union – NextGenerationEU under the Italian Ministry of University and Research (MUR) National Innovation Ecosystem grant ECS00000041 – VITALITY. F. D. A. acknowledges the Università degli Studi di Perugia and MUR for support within the project Vitality.

References

1 A. Kojima, K. Teshima, Y. Shirai and T. Miyasaka, *J. Am. Chem. Soc.*, 2009, **131**, 6050–6051.
2 B.-M. Bresolin, Y. Park and D. W. Bahnemann, *Catalysts*, 2020, **10**, 709.
3 W. Zhang, G. E. Eperon and H. J. Snaith, *Nat. Energy*, 2016, **1**, 16048.
4 X.-K. Liu, W. Xu, S. Bai, Y. Jin, J. Wang, R. H. Friend and F. Gao, *Nat. Mater.*, 2021, **20**, 10–21.
5 H. Huang, B. Pradhan, J. Hofkens, M. B. J. Roeffaers and J. A. Steele, *ACS Energy Lett.*, 2020, **5**, 1107–1123.
6 K. Ren, S. Yue, C. Li, Z. Fang, K. A. M. Gasem, J. Leszczynski, S. Qu, Z. Wang and M. Fan, *J. Mater. Chem. A*, 2022, **10**, 407–429.
7 L. Romani and L. Malavasi, *ACS Omega*, 2020, **5**, 25511–25519.
8 M. Corti, S. Bonomi, R. Chiara, L. Romani, P. Quadrelli and L. Malavasi, *Inorganics*, 2021, **9**, 56.
9 R. Dong, C. Lan, F. Li, S. Yip and J. C. Ho, *Nanoscale Horiz.*, 2019, **4**, 1342–1352.
10 W.-G. Li, X.-D. Wang, J.-F. Liao, Y. Jiang and D.-B. Kuang, *Adv. Funct. Mater.*, 2020, **30**, 1909701.
11 D. Ricciarelli, W. Kaiser, E. Mosconi, J. Wiktor, M. W. Ashraf, L. Malavasi, F. Ambrosio and F. De Angelis, *ACS Energy Lett.*, 2022, 1308–1315.
12 J. Cao and F. Yan, *Energy Environ. Sci.*, 2021, **14**, 1286–1325.
13 M. Chen, M.-G. Ju, H. F. Garces, A. D. Carl, L. K. Ono, Z. Hawash, Y. Zhang, T. Shen, Y. Qi, R. L. Grimm, D. Pacifici, X. C. Zeng, Y. Zhou and N. P. Padture, *Nat. Commun.*, 2019, **10**, 16.
14 P. Cheng, T. Wu, J. Liu, W.-Q. Deng and K. Han, *J. Phys. Chem. Lett.*, 2018, **9**, 2518–2522.
15 A. Abate, *Joule*, 2017, **1**, 659–664.
16 J. Li, H.-L. Cao, W.-B. Jiao, Q. Wang, M. Wei, I. Cantone, J. Lü and A. Abate, *Nat. Commun.*, 2020, **11**, 310.
17 N. K. Noel, S. D. Stranks, A. Abate, C. Wehrenfennig, S. Guarnera, A.-A. Haghighirad, A. Sadhanala, G. E. Eperon, S. K. Pathak, M. B. Johnston, A. Petrozza, L. M. Herz and H. J. Snaith, *Energy Environ. Sci.*, 2014, **7**, 3061–3068.
18 C. Ponti, G. Nasti, D. Di Girolamo, I. Cantone, F. A. Alharthi and A. Abate, *Trends Ecol. Evol.*, 2022, **37**, 281–283.
19 A. Weis, P. Ganswindt, W. Kaiser, H. Illner, C. Maheu, N. Glück, P. Dörflinger, M. Armer, V. Dyakonov, J. P. Hofmann, E. Mosconi, F. De Angelis and T. Bein, *J. Phys. Chem. C*, 2022, **126**, 21040–21049.
20 Z. Jin, Z. Zhang, J. Xiu, H. Song, T. Gatti and Z. He, *J. Mater. Chem. A*, 2020, **8**, 16166–16188.
21 B.-B. Yu, M. Liao, J. Yang, W. Chen, Y. Zhu, X. Zhang, T. Duan, W. Yao, S.-H. Wei and Z. He, *J. Mater. Chem. A*, 2019, **7**, 8818–8825.
22 R. Waykar, A. Bhorde, S. Nair, S. Pandharkar, B. Gabhale, R. Aher, S. Rondiya, A. Waghmare, V. Doiphode, A. Punde, P. Vairale, M. Prasad and S. Jadkar, *J. Phys. Chem. Solids*, 2020, **146**, 109608.
23 M. Pazoki, M. B. Johansson, H. Zhu, P. Broqvist, T. Edvinsson, G. Boschloo and E. M. J. Johansson, *J. Phys. Chem. C*, 2016, **120**, 29039–29046.

24 D. Liu, B.-B. Yu, M. Liao, Z. Jin, L. Zhou, X. Zhang, F. Wang, H. He, T. Gatti and Z. He, *ACS Appl. Mater. Interfaces*, 2020, **12**, 30530–30537.
25 S. Ghosh, S. Mukhopadhyay, S. Paul, B. Pradhan and S. K. De, *ACS Appl. Nano Mater.*, 2020, **3**, 11107–11117.
26 G. Chen, P. Wang, Y. Wu, Q. Zhang, Q. Wu, Z. Wang, Z. Zheng, Y. Liu, Y. Dai and B. Huang, *Adv. Mater.*, 2020, **32**, 2001344.
27 Y. Dai, C. Poidevin, C. Ochoa-Hernández, A. A. Auer and H. Tüysüz, *Angew. Chem., Int. Ed.*, 2020, **59**, 5788–5796.
28 J. S. Han, Q. V. Le, H. Kim, Y. J. Lee, D. E. Lee, I. H. Im, M. K. Lee, S. J. Kim, J. Kim, K. J. Kwak, M.-J. Choi, S. A. Lee, K. Hong, S. Y. Kim and H. W. Jang, *Small*, 2020, **16**, 2003225.
29 S. S. Bhosale, A. K. Kharade, E. Jokar, A. Fathi, S. Chang and E. W.-G. Diau, *J. Am. Chem. Soc.*, 2019, **141**, 20434–20442.
30 Y. Dai and H. Tüysüz, *ChemSusChem*, 2019, **12**, 2587–2592.
31 L. Romani, A. Speltini, C. N. Dibenedetto, A. Listorti, F. Ambrosio, E. Mosconi, A. Simbula, M. Saba, A. Profumo, P. Quadrelli, F. De Angelis and L. Malavasi, *Adv. Funct. Mater.*, 2021, **31**, 2104428.
32 C. Tedesco and L. Malavasi, *Molecules*, 2023, **28**, 339.
33 M. Medina-Llamas, A. Speltini, A. Profumo, F. Panzarea, A. Milella, F. Fracassi, A. Listorti and L. Malavasi, *Nanomaterials*, 2023, **13**, 263.
34 A. Pradhan, M. K. Jena and S. L. Samal, *ACS Appl. Energy Mater.*, 2022, **5**, 6952–6961.
35 Z. Ma, Z. Shi, D. Yang, F. Zhang, S. Li, L. Wang, D. Wu, Y. Zhang, G. Na, L. Zhang, X. Li, Y. Zhang and C. Shan, *ACS Energy Lett.*, 2020, **5**, 385–394.
36 S. Bonomi, P. Galinetto, M. Patrini, L. Romani and L. Malavasi, *Inorg. Chem.*, 2021, **60**, 14142–14150.
37 P. Liu, Y. Liu, S. Zhang, J. Li, C. Wang, C. Zhao, P. Nie, Y. Dong, X. Zhang, S. Zhao and G. Wei, *Adv. Opt. Mater.*, 2020, **8**, 2001072.
38 Z. Zheng, Q. Hu, H. Zhou, P. Luo, A. Nie, H. Zhu, L. Gan, F. Zhuge, Y. Ma, H. Song and T. Zhai, *Nanoscale Horiz.*, 2019, **4**, 1372–1379.
39 S. K. Shil, F. Wang, K. O. Egbo, Z. Lai, Y. Wang, Y. Wang, D. Zhao, S.-W. Tsang, J. C. Ho and K. M. Yu, *ACS Appl. Mater. Interfaces*, 2021, **13**, 35930–35940.
40 H.-H. Zhang, Z.-C. Zhou, Y.-J. Dong, L. Zhang, H.-Y. Chen and D.-B. Kuang, *Sol. RRL*, 2021, **5**, 2100559.
41 C. Lu, D. S. Itanze, A. G. Aragon, X. Ma, H. Li, K. B. Ucer, C. Hewitt, D. L. Carroll, R. T. Williams, Y. Qiu and S. M. Geyer, *Nanoscale*, 2020, **12**, 2987–2991.
42 Y. Hai, W. Huang, Z. Li, D. Wu, Q. Huang and X. Tang, *ACS Appl. Energy Mater.*, 2021, **4**, 5913–5917.
43 Y. Wang, Q. Zhou, Y. Zhu and D. Xu, *Appl. Catal., B*, 2021, **294**, 120236.
44 H. Wang, B. Zhou and W. Li, *Phys. Chem. Chem. Phys.*, 2023, **25**, 486–493.
45 K. M. Boopathi, P. Karuppuswamy, A. Singh, C. Hanmandlu, L. Lin, S. A. Abbas, C. C. Chang, P. C. Wang, G. Li and C. W. Chu, *J. Mater. Chem. A*, 2017, **5**, 20843–20850.
46 A. Singh, S. Najman, A. Mohapatra, Y.-J. Lu, C. Hanmandlu, C.-W. Pao, Y.-F. Chen, C. S. Lai and C.-W. Chu, *ACS Appl. Mater. Interfaces*, 2020, **12**, 32649–32657.
47 K. Ahmad, P. Kumar and S. M. Mobin, *Chem. – Asian J.*, 2020, **15**, 2859–2863.
48 Z. Li, S. R. Kavanagh, M. Napari, R. G. Palgrave, M. Abdi-Jalebi, Z. Andaji-Garmaroudi, D. W. Davies, M. Laitinen, J. Julin, M. A. Isaacs, R. H. Friend, D. O. Scanlon, A. Walsh and R. L. Z. Hoye, *J. Mater. Chem. A*, 2020, **8**, 21780–21788.
49 Y. El Ajjouri, V. S. Chirvony, N. Vassilyeva, M. Sessolo, F. Palazon and H. J. Bolink, *J. Mater. Chem. C*, 2019, **7**, 6236–6240.
50 D. Samanta, S. P. Chaudhary, B. Ghosh, S. Bhattacharyya, G. Shukla and G. D. Mukherjee, *Phys. Rev. B*, 2022, **105**, 104103.
51 Y. Zhang, J. Yin, M. R. Parida, G. H. Ahmed, J. Pan, O. M. Bakr, J.-L. Brédas and O. F. Mohammed, *J. Phys. Chem. Lett.*, 2017, **8**, 3173–3177.
52 J. Gu, G. Yan, Y. Lian, Q. Mu, H. Jin, Z. Zhang, Z. Deng and Y. Peng, *RSC Adv.*, 2018, **8**, 25802–25807.
53 S. Rieger, B. J. Bohn, M. Döblinger, A. F. Richter, Y. Tong, K. Wang, P. Müller-Buschbaum, L. Polavarapu, L. Leppert, J. K. Stolarczyk and J. Feldmann, *Phys. Rev. B*, 2019, **100**, 201404.
54 A. Goyal, S. McKechnie, D. Pashov, W. Tumas, M. Van Schilfgaarde and V. Stevanovic, *Chem. Mater.*, 2018, **30**, 3920–3928.
55 B. Saparov, F. Hong, J.-P. Sun, H.-S. Duan, W. Meng, S. Cameron, I. G. Hill, Y. Yan and D. B. Mitzi, *Chem. Mater.*, 2015, **27**, 5622–5632.
56 K. Yamada, H. Sera, S. Sawada, H. Tada, T. Okuda and H. Tanaka, *J. Solid State Chem.*, 1997, **134**, 319–325.
57 K. M. McCall, C. C. Stoumpos, S. S. Kostina, M. G. Kanatzidis and B. W. Wessels, *Chem. Mater.*, 2017, **29**, 4129–4145.